# Kinematically Stabilized Microbubble Actuator Arrays

Xiaosong Wu, Guang Yuan, Yong-Kyu Yoon, *Member, IEEE*, and Mark G. Allen, *Senior Member, IEEE*

***Abstract*—In this paper, the concept, fabrication, and characterization of a kinematically stabilized polymeric microbubble actuator (endoskeletal microbubble actuator) for a pneumatic tactile display application are presented. The kinematic stabilization is achieved by the combination of two polymeric layers with complementary functions: a microcorrugated parylene diaphragm layer as a "skeleton" to provide a directional deflection in a desired axial direction while suppressing undesired lateral deflections and an overcoated elastomer diaphragm layer as a "skin" to help the extended membrane recoil to its original shape, ensuring diaphragm stability. Arrays of microcorrugated diaphragms are implemented in a mass producible fashion using inclined rotational UV lithography, micromolding, and pattern transfer techniques. Both the number of corrugations and the corrugation profile of the endoskeletal actuator are determined through numerical analysis, taking into account the constraints of the microfabrication processes utilized. A prototype of a single endoskeletal bubble actuator with a diameter of 2.6 mm has been fabricated and characterized. For comparison purposes, elastomer microcorrugated diaphragm (skin only) actuators and parylene microcorrugated diaphragm (skeleton only) actuators of the same materials and dimensions have also been fabricated and tested. While the skin-only diaphragm actuators demonstrated undesired omnidirectional inflation and the skeleton-only diaphragm actuators have shown unstable and irreversible deformation during extension, the proposed endoskeletal microbubble actuators have shown stable reversible axial extensions with a deflection of approximately 0.9 mm. A $6 \times 6$ array of endoskeletal polymer microbubble actuators integrated with a microfluidic manifold has been successfully fabricated, demonstrating its mass manufacturability. [2006-0243]**

***Index Terms*—Digital Clay, endoskeletal bubble, inclined exposure, microbubble actuator, microcorrugated diaphragm.**

## I. Introduction

While current computer–human interaction relies much on audio and visual effects, the additional usage of real-time interactive 3-D haptic interfaces has the potential to become a revolutionary means of communication for many areas of engineering, art, science, and medical diagnosis. Such a "Digital Clay" interface would enable both user-specified display of shapes as output from a computer and user-directed input of shapes to a computer. A description of "Digital Clay," including various potential implementations of the clay, is given in [1].

Digital Clay can be considered as a touch-based distributed input/display device. High resolution is sought by using microelectromechanical systems (MEMS) technology to produce valves, sensors, and actuators. A critical concern is the nature of the actuators that gives Digital Clay the power to alter its shape and to exert a resistive force upon user's hands. Actuators for Digital Clay must possess the following attributes: 1) ability to generate large deflections for tactile input/output; 2) ability to generate large forces to interact with human input; and 3) ability to be mass-manufactured so that large arrays can be inexpensively formed. In order to achieve the desired balance between the required power and degree of miniaturization, a MEMS-compatible hydraulically or pneumatically driven microbubble actuator array is opted for. In this approach, the surface of Digital Clay is defined by an actuated kinematic structure, i.e., microbubbles. Each individual microbubble actuator forms a tactile "pixel" in the Digital Clay structure.

Previously, several types of pneumatic microactuators have been fabricated using the MEMS technology. Among them, microballoons made up of elastomer, such as silicone rubber or polyurethane (PU), have the advantages of a relatively simple structure and fabrication sequence while being capable of large deflection, as shown in Fig. 1(a). These actuators have been used in end effectors [2], acoustic impedance control [3], aerodynamic control [4], and a microfinger [5]. However, balloons typically deflect omnidirectionally into a spherical shape, which makes them undesirable for Digital Clay applications requiring more directional or linear movements. Furthermore, the relationship between pressure and radius is nonmonotonic for balloon actuators, which raises instability issues when a pure balloon actuator is either intentionally or accidentally hyperinflated [6]. Research on actuators with large and stable deflections in preferential directions is necessary.

Bellows actuators with corrugated sidewalls characteristically have a large linear deflection in their axial direction. Their implementation in the vertical dimension using micromachining techniques has been demonstrated [7], [8]. For these vertical devices, however, the complexity of fabrication and process time increase as the number of corrugations of the bellows increases. Alternatively, a corrugated diaphragm made up of nonelastomeric material with relatively high modulus can be used to achieve axial deflection preferentially, as shown in Fig. 1(b). Corrugated diaphragms are widely used in altimeters, pressure gauges, speakers, and other applications that require

Manuscript received November 2, 2006; revised August 6, 2007. This work was supported in part by the National Science Foundation "Digital Clay" project under Contract IIS-0121663. Subject Editor K. Bohringer.

X. Wu is with the School of Polymer, Textile and Fiber Engineering, Georgia Institute of Technology, Atlanta, GA 30332 USA (e-mail: sharonwu@gatech.edu).

G. Yuan and M. G. Allen are with the School of Electrical and Computer Engineering, Georgia Institute of Technology, Atlanta, GA 30332 USA.

Y.-K. Yoon is with the Department of Electrical Engineering, State University of New York, Buffalo, NY 14260 USA.

Color versions of one or more of the figures in this paper are available online at http://ieeexplore.ieee.org.

Digital Object Identifier 10.1109/JMEMS.2007.911868

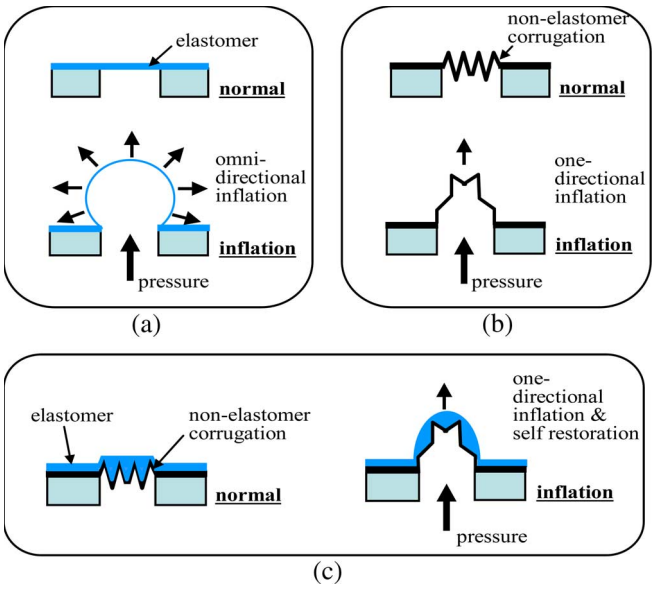


Fig. 1. Device concept: (a) Elastomer diaphragm actuator, (b) nonelastomer-based microcorrugated diaphragm actuator, and (c) endoskeletal bubble actuator.

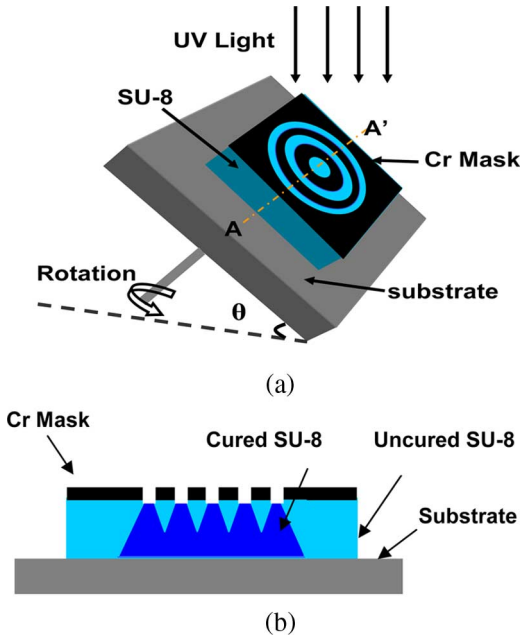


Fig. 2. Continuously rotating inclined exposure for concentrically corrugated diaphragm with slanted side walls: (a) Exposure scheme and (b) cross-sectional view of $A - A'$.

large linear deflections. MEMS-based parylene corrugated diaphragms have been reported in the applications of pressure transducer and electromagnetic actuator [9], [10]. However, applications such as Digital Clay require even larger deflection of corrugated diaphragms, which could not be achieved though parylene corrugated diaphragms because they often have poor self-restoration properties under a large deflection. When large deformation occurs, parylene corrugated diaphragms can reach a local stability point, not being able to return to the original position even after the removal of the external pressure.

In this paper, we present a mass-manufacturable endoskeletal microbubble actuator capable of reversible vertical deflection. In our approach, microcorrugated nonelastomeric (parylene) diaphragms are embedded under soft elastomer (PU) membranes during the fabrication process to form a skeleton, as shown in Fig. 1(c). The corrugated shape of the skeleton limits the deflection to be primarily in the desired direction. The elastomer acts to promote the "spring back" mechanism of the corrugated diaphragm, thereby enhancing the linearity and reversible expansion of the actuator even to the full extent of the corrugations. Applications of such a structure extend beyond the Digital Clay and may include passive pressure gauges and sensitive pressure sensors. In this paper, the skeletal corrugated sections of the microbubble array are obtained using a single lithographic mask through a continuously rotating inclined exposure [11]–[13], followed by sacrificial material molding and parylene coating. This approach not only makes endoskeletal bubble actuators mass-manufacturable but also can be scaled down to even smaller dimensions if required.

## II. Concept and Design

### A. Design of the Corrugation Profile

Commonly used corrugation profiles include "sinusoidal," "trapezoidal," "triangular," "rectangular," and "toroidal" [14] profiles. Sinusoidal and toroidal profiles are difficult to obtain by conventional MEMS technology because of the round surfaces. The rectangular profile can be obtained by a single lithography process. However, the rectangular profile has the largest flexural stiffness in the tangential direction compared with other profiles. In addition, such profile adds difficulties to mold release. Therefore, the triangular and trapezoidal profiles are considered for microcorrugation.

In this paper, a combination of triangular and trapezoidal profiles is obtained using a continuously rotating inclined UV exposure technique, as shown in Fig. 2 [15], [16]. The mask layout for corrugation fabrication contains six concentric dark circles. A photopatternable negative tone epoxy (SU-8, Microchem, Inc.) is spin-coated on a glass substrate and soft-baked. The substrate is mounted on a rotational stage with an inclined angle $\theta$. An appropriate optical dose of UV exposure in a rotational mode [Fig. 2(a)] is carried out after the mask with a concentric circular pattern is placed on the substrate. After post-exposure baking and development of the substrate, a combination of triangular (lower portion of the tooth) and trapezoidal (upper portion of the tooth) profiles is obtained, which is shown in Fig. 2(b) [the cross-sectional view of $A - A'$ in Fig. 2(a)]. The dimensions of the corrugations are determined by the width and intervals between two concentric circles as well as the inclined angle.

### B. Design of the Number and Angle of the Corrugation

A diameter of 2.6 mm has been selected first for the bubble actuator to meet the requirement for Digital Clay. One of the major concerns about a corrugated diaphragm in many applications is the mechanical sensitivity (defined by displacement per unit applied pressure). In this paper, the maximal achievable deflection is also of great interest. The maximal achievable

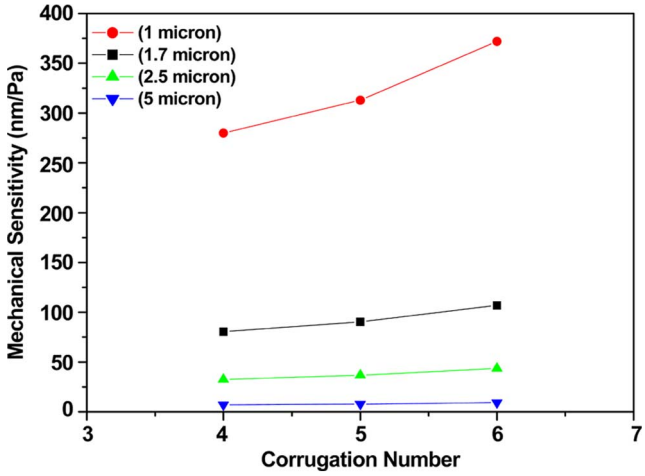


Fig. 3. Mechanical sensitivity as functions of corrugation number and thickness of parylene microcorrugated diaphragm.

deflection increases with both the number of corrugations and the corrugation depth. The number of corrugations can be changed by simply modifying the photomask design. Note that with a given outer diameter of the diaphragm, the increase of the number of corrugations results in the reduction of the corrugation width.

Because the fabrication of the corrugated diaphragm is accomplished through rotational inclined exposure, the corrugation depth is determined by the width of the dark circular pattern on the photomask and the inclined angle. In order to increase the corrugation depth, the inclined angle has to be decreased (i.e., steeper sidewall), resulting in an acute angle of each corrugation tooth that leads to difficulties in subsequent demolding processes, such as increased susceptibility to mechanical instability and mechanical insensitivity due to relatively vertical sidewall with limited lateral working space. After testing various structures with various angles between 15° and 30°, an inclined angle of 17° was chosen as the second parameter for the diaphragm design, which provides both relatively large deflection and fabrication stability.

Next, the mechanical sensitivities of various devices as functions of corrugation number and diaphragm thickness at a pressure load of 100 Pa have been investigated using a finite-element analysis (FEA) tool (ANSYS v.8.0, Ansoft, Inc.). The results are shown in Fig. 3. A 2-D sxial symmetrical model is utilized for the corrugated diaphragm. In general, the diaphragm sensitivity increases as the corrugation number increases for all the four diaphragms with different thicknesses. However, as the thickness goes beyond 2.5 $\mu$m, the variation in the corrugation number only has a negligible effect on the resulting mechanical sensitivity of corrugated diaphragms. The sensitivity is approximately inversely proportional to the square of the diaphragm thickness, as also observed in silicon nitride corrugated diaphragm. [17]. Because of its large sensitivity and large deflection, a profile with six corrugations was selected. The preferred thickness of the diaphragm is less than 2.5 $\mu$m.

A design of diaphragm with six corrugations, an inclined angle of 17°, and a diameter of 2.6 mm have been adopted for the fabrication of endoskeletal microbubble actuators. Deeper corrugations in the center of the diaphragm enhance the vertically oriented center deflection. The schematic view of the corrugated diaphragm is shown in Fig. 4, and the dimensions are listed in Table I.

## III. Materials

The skeleton material, from which the corrugated diaphragm will be made, should be flexible in order to provide large deflection. And the skin material should have high elasticity and an even lower Young's modulus than the skeleton material so that the overall stiffness will be dominated by the skeletal material.

Parylene C (poly-monochloro-para-xylylene) has been selected as the skeleton material due to its low Young's modulus and conformal coating capability over microstructures [18]. Moreover, its low permeability to gas and moisture and high chemical resistance make it desirable for the application of pneumatic and hydraulic actuators.

Ideally, the material of the skin should be highly compliant and elastic. However, all natural and synthetic elastomers are viscoelastic. While they show a much larger elastic region than other inorganic materials or thermoplastics, the deformation curve within the elastic region is not linear. In addition, a large hysteresis loop is observed during cyclic testing. The mechanical properties of two types of common castable elastomers, polydimethylsiloxane (PDMS, Sylgard 184, Dow Corning) and PU (Poly 74-20, Polytek), particularly elastic and hysteresis properties, are characterized by static tensile tests. The mechanical properties of parylene C thin film have also been characterized. Table II lists the mechanical properties of parylene C and elastomers (PDMS and PU). PU was chosen in our application because of its extremely low Young's modulus, large elongation at break, and small hysteresis.

## IV. Numerical Analysis

The FEA simulation results of the center displacement of three endoskeletal microbubble actuators as functions of applied pressure are determined from the ANSYS finite element program and are shown in Fig. 5. Two ANSYS element types are used in the simulation. One is plane 82 for parylene, and the other is hyper 84 for PU elastomer. Plane 82 is a 2-D eight-node structural solid element with large strain capability, and hyper 84 is a hyperelastic solid element based on Mooney–Rivlin nonlinear elastic model [19]. The Mooney–Rivlin constants used in ANSYS simulation are derived from the stress–strain curve obtained by a uniaxial tensile test. These three endoskeletal bubble actuators are with 2-$\mu$m-thick parylene and 100-$\mu$m-thick PU, with 2-$\mu$m-thick parylene and 200-$\mu$m-thick PU, and with 5-$\mu$m-thick parylene and 100-$\mu$m-thick PU. The deflection curves for the two actuators having the same parylene thickness but different PU thickness are adjacent close to each other. However, the slopes of the curves of the two actuators with different parylene thickness but identical PU thickness are much different. It is concluded that the mechanical stiffness of the endoskeletal bubble actuator is dominated by the thickness of parylene.

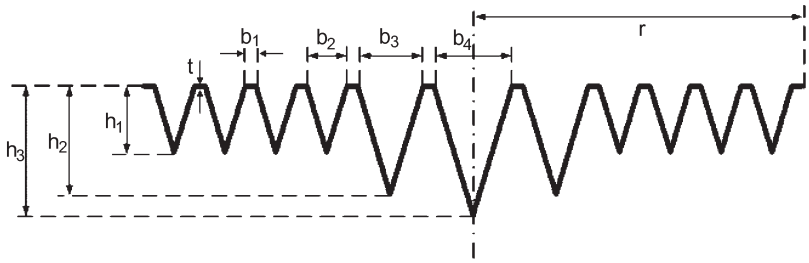


Fig. 4. Schematic cross-sectional view of a corrugated diaphragm with six corrugations.

TABLE I
CHARACTERISTIC DIMENSIONS OF THE CORRUGATION DIAPHRAGM WITH SIX CORRUGATIONS

| Symbol | t | r | $b_1$ | $b_2$ | $b_3$ | $b_4$ | $h_1$ | $h_2$ | $h_3$ |
|---|---|---|---|---|---|---|---|---|---|
| Dimension (mm) | 0.002<br>0.005 | 1.3 | 0.05 | 0.15 | 0.25 | 0.3 | 0.245 | 0.409 | 0.491 |

TABLE II
MECHANICAL PROPERTIES OF CANDIDATE POLYMER MATERIALS FROM TENSILE TEST

| | Young's Modulus (MPa) | Tensile strength (MPa) | Elongation at break (%) | Yield Strength (MPa) | Yield elongation (%) |
|---|---|---|---|---|---|
| Parylene | 2000 | 68 | 200[19] | 68 | 3.7 |
| PU | 0.26 | 0.86 | 600 | / | / |
| PDMS | 1.18 | 6.27 | 250 | / | / |

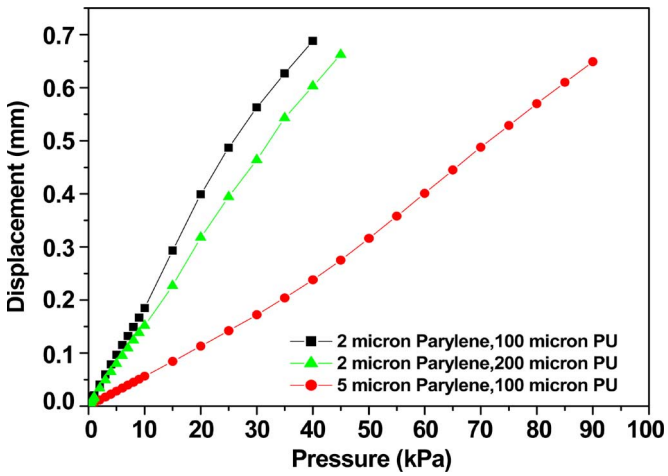


Fig. 5. Computed results of center displacement of the endoskeletal bubble actuators with composite diaphragms of 2-$\mu$m-thick parylene and 100-$\mu$m-thick PU, 2-$\mu$m-thick parylene and 200-$\mu$m-thick PU, and 5-$\mu$m-thick parylene and 100-$\mu$m-thick PU.

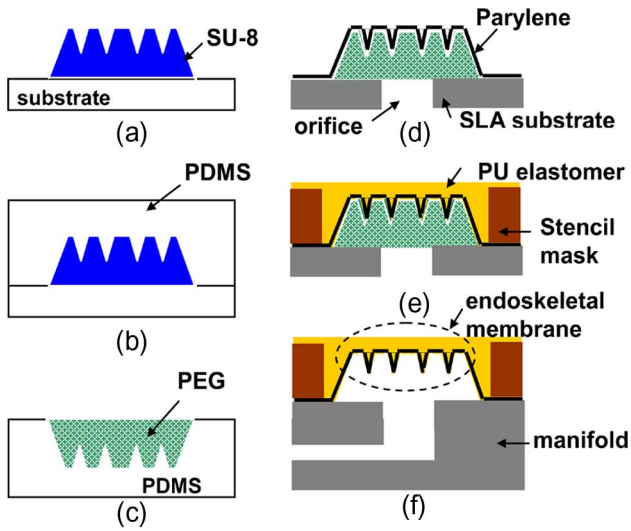


Fig. 6. Overall fabrication process.

## V. FABRICATION

### A. SU-8 Micromold for Corrugated Diaphragms

Fig. 6 shows the overall fabrication process of the endoskeletal microbubble actuators. A master pattern of the corrugated diaphragms, as described in the previous section, is fabricated using SU-8 [Fig. 6(a)].

### B. Transfer Molding of Sacrificial Polyethylene Glycol (PEG) Micromold

A 10 : 1 mixture of PDMS elastomer base and curing agent is well mixed and degassed and then cast onto the SU-8 master pattern to obtain a negative replica [Fig. 6(b)]. After curing at room temperature for 24 h, the PDMS negative is

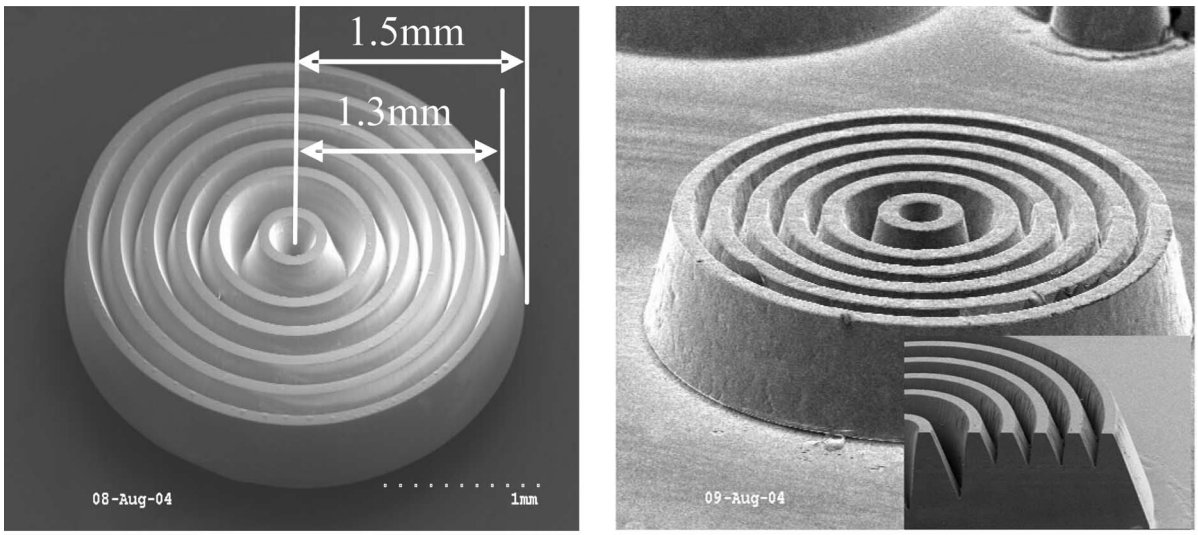


(a) (b)

Fig. 7. Comparison of (a) SU-8 mold and (b) replicated PEG mold: inset shows a cross-sectional image of the corrugation profile.

separated from the substrate. A sacrificial material (PEG wax, Kindt Collins) is cast into the PDMS mold [Fig. 6(c)] in its molten state at 60 °C. Excess PEG is scrapped off the surface of the mold. An epoxy acrylate substrate having a matching orifice array pattern with the corrugation array is fabricated by stereolithography (SLA) using a photocurable liquid epoxy acrylate resin (Renshape SL7510, Huntsman). The PEG corrugation array is aligned and bonded onto the epoxy substrate. During the transfer step, the PEG is kept at a soft state to provide good adhesion. After attached to the epoxy orifice array, the PEG is allowed to cool down to a room temperature and harden. The PDMS mold is peeled off from the SLA substrate, with the PEG corrugation replica left on the substrate.

### C. Fabrication of Corrugated Diaphragms

Three different types of diaphragms are fabricated: parylene corrugated diaphragm (skeleton only), PU elastomer corrugated diaphragm (skin only), and endoskeletal bubble.

*1) Parylene Corrugated Diaphragm:* A parylene layer is conformally coated to the PEG corrugation array [Fig. 6(d)]. The sacrificial PEG is removed by dissolving in water to release the parylene corrugated diaphragm.

*2) PU Elastomer Corrugated Diaphragm:* A stencil mask fabricated by SLA is placed on the epoxy substrate to level the top surface. A thin layer of the PU elastomer is then spin-coated on top of the corrugated surface [Fig. 6(e)]. The elastomer is cured at room temperature, and the sacrificial PEG is removed by dissolving in water.

*3) Endoskeletal Bubble:* A parylene layer is conformally coated to the PEG corrugation array to form the corrugated skeletal diaphragm [Fig. 6(d)]. A stencil mask is placed on the epoxy substrate to level the top surface. A thin layer of PU elastomer is then spin-coated on top of the corrugated surface [Fig. 6(e)]. The elastomer is cured at room temperature, and the sacrificial PEG is removed by dissolving in water to form endoskeletal bubbles.

### D. Bonding and Assembly

A manifold with 36 fluidic channels is fabricated by SLA. The epoxy substrate with a $6 \times 6$ diaphragm array is bonded to the manifold so that each actuator can be addressed independently [Fig. 6(f)].

SEM photomicrographs of a single corrugated SU-8 master pattern and a corresponding PEG replica pattern are shown in Fig. 7. The top diameter, the bottom diameter, and the height of the diaphragm are 2.6 mm, 3.0 mm, and 600 $\mu$m, respectively. An incident angle $\theta$ of 30° of a UV light results in a refracted angle of approximately 17° of the slanted sidewall of the corrugation. The depths of the corrugations are listed in Table I. The molded PEG structure faithfully follows the original SU-8 microcorrugation, as shown in Fig. 7, the inset of which shows the cross-sectional view of the combinational corrugation with a trapezoidal shape on top and a triangular shape on bottom. Fig. 8(a) and (b) shows an SU-8 microcorrugated mold array and a batch-transferred corrugated PEG mold array mounted on a stereolithographically fabricated manifold substrate, respectively.

## VI. Testing and Results

Diaphragm center deflection as a function of applied pressure has been quantitatively characterized. Compressed air is applied to the diaphragm through the manifold channels, and the diaphragm displacement is measured using a laser displacement sensor (LK-G32, KEYENCE Co.). Comparison experiments have also been carried out on parylene corrugated diaphragm (skeleton only) and PU elastomer corrugated diaphragm (skin only). The inflated shapes of diaphragms are captured by a video microscope.

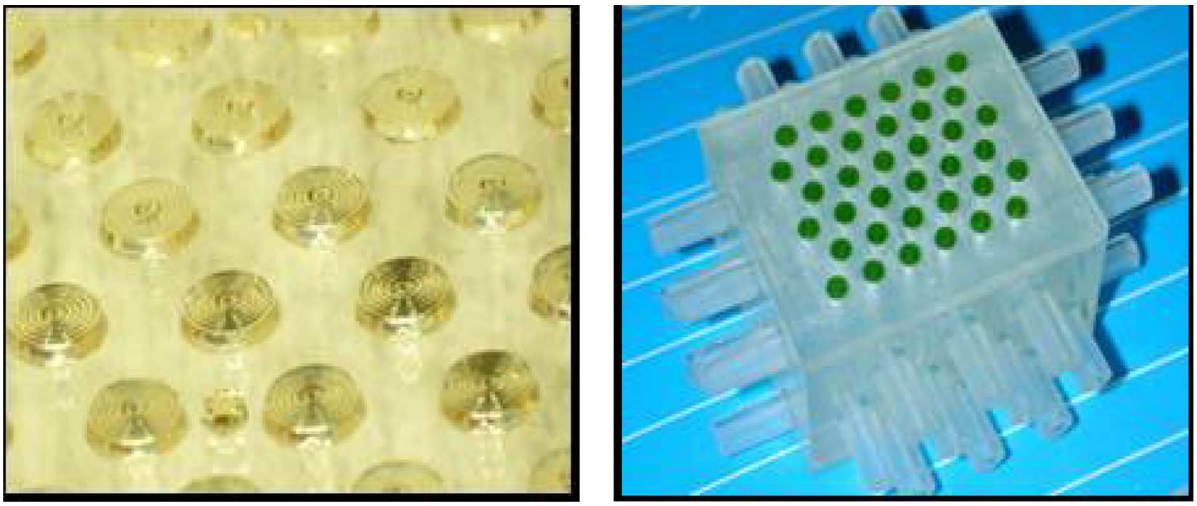

(a) (b)

Fig. 8. Corrugated pattern array: (a) SU-8 master pattern array and (b) batch-transferred corrugated PEG corrugation array on an SLA manifold substrate.

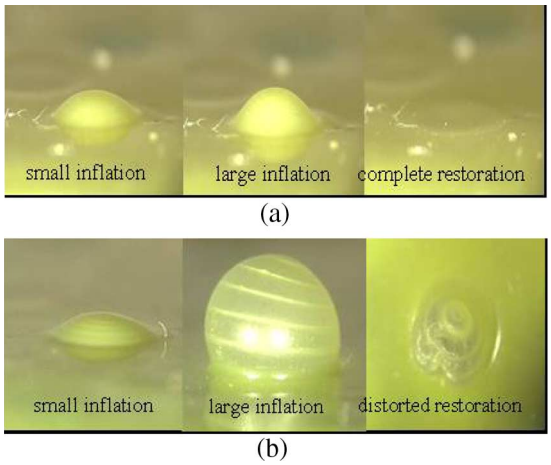


Fig. 9. Inflated shape comparison of (a) endoskeletal bubble and (b) PU elastomer diaphragm.

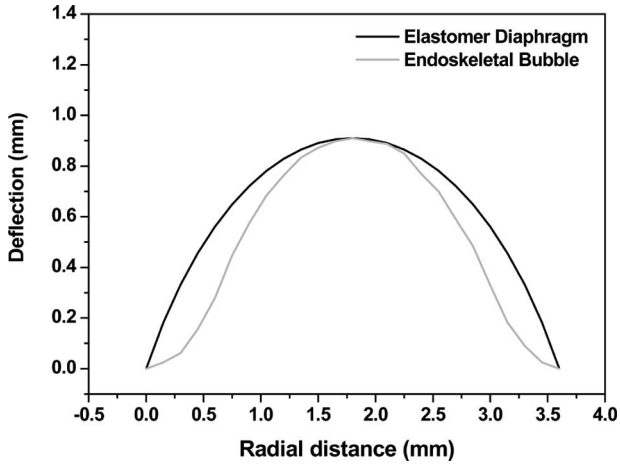


Fig. 10. Comparison of the cross-sectional area of the inflated endoskeletal bubble and PU elastomer diaphragm.

### A. *Inflated Shape*

Fig. 9 shows the inflated and restored shapes for an endoskeletal bubble actuator [Fig. 9(a)] and a PU elastomer diaphragm (skin-only) [Fig. 9(b)]. For the endoskeletal bubble, the inflation of the diaphragm is confined to one direction, i.e., out of plane, and the displacement is a reasonably linear function of the applied pressure. After the applied pressure is removed, the diaphragm returns to its original position and shape. The PU elastomer diaphragm shows similar stability and a spherical shape at small deflection but an omnidirectional balloonlike expansion at large deflection, resulting in plastic deformation of the material. Note that when the diaphragm is deflated by removing the applied pressure, it becomes flaccid and does not return to its original shape. The cross sections of the deformed shapes of an endoskeletal bubble actuator and a PU elastomer diaphragm at 0.91-mm deflection are compared in Fig. 10. The cross-sectional area under the profile of the endoskeletal bubble actuator is 80.7% of that of under the profile of the PU elastomer diaphragm.

### B. *Static Testing*

The static pressure-deflection characteristics are tested for the parylene diaphragm, PU elastomer diaphragm, and endoskeletal bubble. The thicknesses of the parylene diaphragm and PU elastomer diaphragm are 5 and 150 $\mu$m, respectively. The endoskeletal bubble actuator has parylene and PU layers with the same thicknesses as those of the parylene diaphragm and PU elastomer diaphragm. The results are shown in Fig. 11. Among the three actuators compared, the PU elastomer diaphragm has an extremely low Young's modulus and requires the smallest pressure to achieve a given deflection. The endoskeletal bubbles require the largest pressure for the same deflection because they consist of a composite of two materials—PU and parylene—each layer of the composite having the same thickness as that of the other two diaphragms, thereby resulting in the largest effective stiffness.

The distinct "jumps" in the pressure-deflection curve for the parylene diaphragm indicate "unfolds" of one or more corrugations, which results in the large deflection. The unfolded

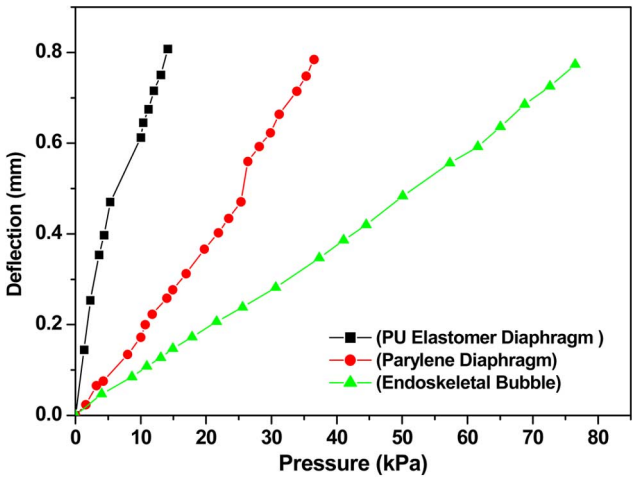


Fig. 11. Diaphragm deflection as functions of the applied pressure for three actuators: PU elastomer diaphragm, parylene diaphragm, and endoskeletal bubble.

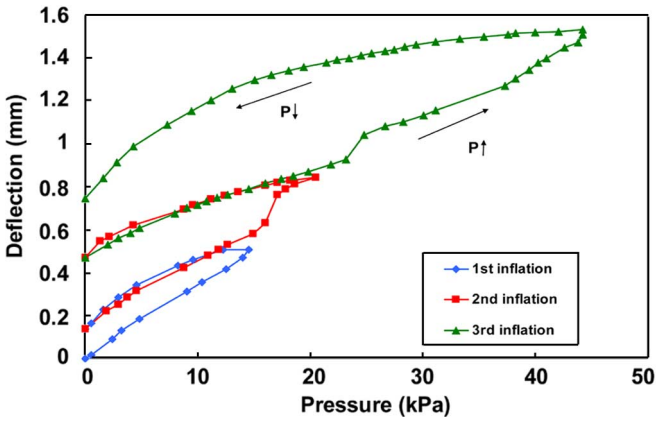


Fig. 12. Center displacement as a function of the applied pressure load of a parylene diaphragm in cyclic testing. In the first inflation, a parylene diaphragm is loaded until the center displacement is 0.48 mm. The second inflation cycle reaches a center displacement of 0.75 mm, and the third one reaches 1.46 mm.

corrugation does not always "refold" upon release of pressure because the unfolding has led to another minimum energy state. The addition of elastomer greatly enhances the linearity in the pressure-deflection relationship of the endoskeletal bubbles while maintaining the unidirectional deflection of the actuator.

### C. Cyclic Testing

The performance of the three types of the aforementioned actuators undergoing cyclic inflation and deflation at a constant low rate is tested. The relationship between the applied load and the deflection of a parylene diaphragm in cyclic testing is shown in Fig. 12. In the test, a parylene diaphragm is loaded with pressure until the center displacement is 0.48 mm and then deflated. The second inflation cycle reaches a center displacement of 0.75 mm, and the third one reaches 1.46 mm. Three hysteresis loops are observed for the three loading cycles. The hysteresis at small deflection comes from the viscoelastic nature of parylene material. There is no evidence of unfolding of corrugation in the inflation curve of the first loading cycle. The unfolding of corrugation accompanied with the permanent

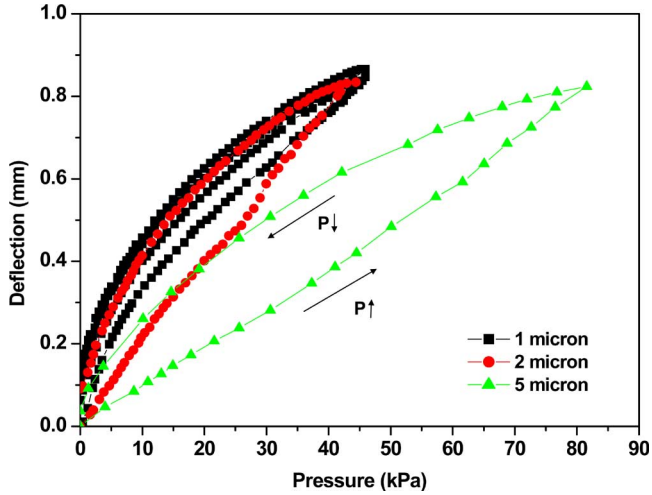


Fig. 13. Cyclic behavior of endoskeletal bubble actuators with the same PU thickness (150 $\mu$m) but different parylene thicknesses (1, 2, and 5 $\mu$m).

deformation of parylene in the second and third loading broadens the hysteresis loops much more. The remnant deflection is irreversible because the unfolding has led to another minimum energy state.

Three endoskeletal bubble actuators with the same PU thickness (150 $\mu$m) but different parylene thicknesses (1, 2, and 5 $\mu$m) are fabricated. Their cyclic behaviors are shown in Fig. 13. The inflation and deflation curves form a hysteresis loop in all the three cases. The hysteresis is defined as the percentage ratio of the difference between two deflections at the midpoint of the applied pressure to the maximum deflection. The values of hysteresis for 1-, 2-, and 5-$\mu$m-thick bubbles are 13%, 24%, and 27%, respectively.

The 1-$\mu$m-thick device shows the least stiffness as well as the lowest hysteresis among the three bubbles. It would be the most desired bubble actuator in our application. However, during test, it is found that 1-$\mu$m-thick devices are insufficiently robust compared to the other two bubbles.

After an initial deformation and recovery cycle, repeated inflation and deflation cycles result in much less hysteresis, demonstrating the functionality of the kinematically stabilized actuator, as can be seen in Fig. 14.

It is hypothesized that the observed hysteresis consists of two components: a plastic deformation of the underlying parylene layer during the initial inflation and a viscoelastic dissipation occurring primarily in the PU elastomer overcoat in subsequent inflations. To test this hypothesis, finite element models are utilized to determine if the plastic limit of parylene is exceeded, particularly in the sharp bends of the corrugation, during the initial inflation. Furthermore, after the initial deflection, the hysteresis performance of the endoskeletal bubbles is compared to the PU elastomer diaphragms to see if any additional hysteretic effects of the endoskeletal bubbles over and above the PU-only diaphragms can be observed.

Fig. 15 shows the calculated stress using the FEA in an endoskeletal bubble actuator with 2-$\mu$m-thick parylene and 150-$\mu$m-thick PU elastomer, under a pressure load of 44 kPa and a center deflection of 0.697 mm. At corners of the trapezoidal-shaped corrugations, the stress exceeds the yield

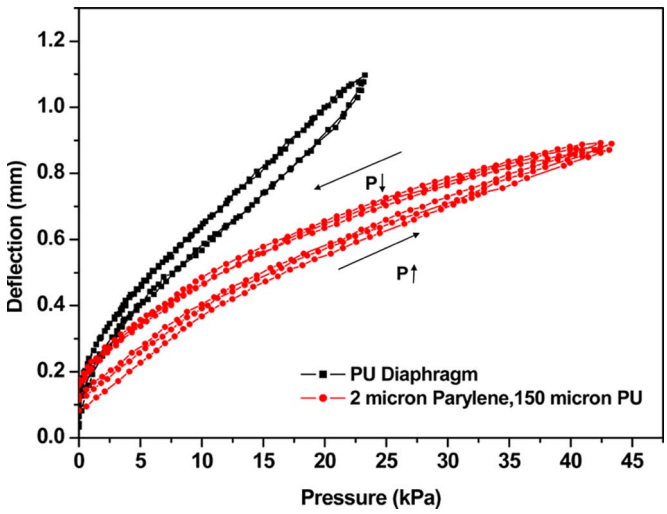


Fig. 14. Displacements in subsequent loading and unloading cycles after an initial deformation and recovery cycle for a PU diaphragm and an endoskeletal bubble actuator with 2-$\mu$m-thick parylene and 150-$\mu$m-thick PU elastomer.

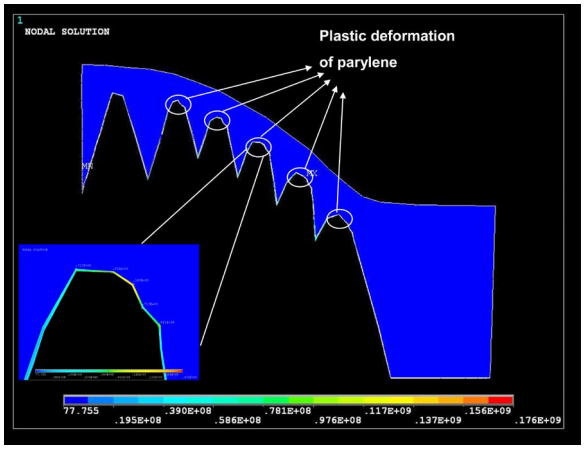


Fig. 15. Calculated stress in an endoskeletal bubble actuator with 2-$\mu$m-thick parylene and 150-$\mu$m-thick PU elastomer with a center deflection of 0.697 mm.

stress of parylene, which is 68 MPa. Approximately 4% of the parylene layer yields at this pressure load.

After the initial inflation, the hysteresis performance of the endoskeletal bubble is compared to that of a PU elastomer diaphragm. As shown in Fig. 14, after the initial inflation, the hysteresis of the 2-$\mu$m-thick endoskeletal bubble actuator is reduced to 8.4%, which is comparable to that of a PU elastomer diaphragm of the same nominal thickness (6.5%, as shown in Fig. 14). The observations, which show that the FEA model predicts the plastic deformation of the parylene layer on the initial inflation and that the hysteresis of the endoskeletal bubble actuator after the initial inflation is comparable to the hysteresis of a PU elastomer diaphragm, are consistent with the hypothesis discussed above.

### *D. Actuator Performance Verification*

To verify the performance of the endoskeletal bubble actuator, the numerical analysis results by ANSYS and the experimental results of each actuator are compared. Fig. 16 shows the center displacement of an endoskeletal bubble actuator as a function of the applied pressure, where a bubble actuator with a 2-$\mu$m-thick parylene and a 150-$\mu$m-thick PU elastomer has been used. The experimental data exhibit good linearity and agree reasonably well with the simulation results. The discrepancy may have resulted from the inaccuracy in the parameters used for the nonlinear elastic model in ANSYS simulation.

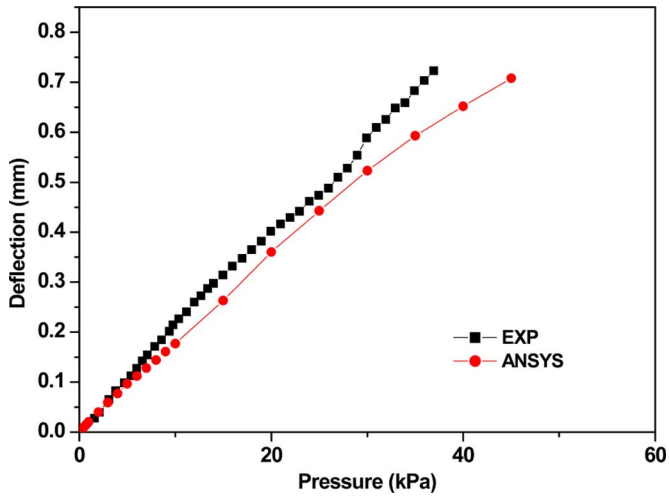


Fig. 16. Comparison of the experimental and FEA results for an endoskeletal bubble actuator with 2-$\mu$m-thick parylene and 150-$\mu$m-thick PU elastomer.

## VII. Conclusion

A pneumatically driven kinematically stabilized endoskeletal bubble actuator has been proposed and implemented for future use in Digital Clay research. The mass-manufacturable actuator has been fabricated using the approaches of lithography and micromolding. The skeletal corrugated sections have been fabricated using a continuous rotating inclined exposure. PU elastomer microcorrugated diaphragm (skin-only) actuators and parylene microcorrugated diaphragm (skeleton-only) actuators with the same profiles have also been fabricated and characterized for comparison. The endoskeletal bubble actuator has demonstrated a stable directional deflection as a function of the applied pressure, and the experimental deflection results show good agreement with those of the FEA.

## Acknowledgment

The authors would like to thank R. Shafer, S.-O. Choi, and Dr. S.-H. Kim in the Georgia Tech Microsensor and Microactuator group for their assistance on the experiments as well as for their valuable technical discussions. Microfabrication was carried out in part in the Georgia Tech Microelectronics Research Center.

## References

[1] J. Rossignac, M. G. Allen, W. J. Book, A. Glezer, I. Ebert-Uphoff, C. Shaw, D. Rosen, S. Askins, J. Bai, P. Bosscher, J. Gargus, B. M. Kim, I. Llamas, A. Nguyen, G. Yuan, and H. Zhu, "Finger sculpting with digital clay: 3D shape input and output through a computer-controlled real surface," in *Proc. Int. Conf. Shape Model., Appl.*, Seoul, Korea, 2003, pp. 229–231.

[2] F. Kawai, P. Cusin, and S. Konishi, "Thin flexible end-effector using pneumatic balloon actuator," in *Proc. 13th Int. Conf. Micro Electro Mech. Syst.*, Miyazaki, Japan, 2000, pp. 391–396.

[3] M. Yoda and S. Konishi, "Acoustic impedance control through structural tuning by pneumatic balloon actuators," in *Proc. 14th Int. Conf. Micro Electro Mech. Syst.*, Interlaken, Switzerland, 2001, pp. 244–247.
[4] C. Grosjean, G. B. Lee, W. Hong, Y. C. Tai, and C. M. Ho, "Micro balloon actuators for aerodynamic control," in *Proc. 11th Int. Conf. Micro Electro Mech. Syst.*, Heidelberg, Germany, 1998, pp. 166–171.
[5] O. C. Jeong and S. Konishi, "All PDMS pneumatic microfinger with bidirectional motion and its application," *J. Microelectromech. Syst.*, vol. 15, no. 4, pp. 896–903, Aug. 2006.
[6] I. Müller and P. Strehlow, *Rubber and Rubber Balloons: Paradigms of Thermodynamics*. Berlin, Germany: Springer-Verlag, 2004, pp. 4–5.
[7] X. Yang, Y. C. Tai, and C. M. Ho, "Micro bellow actuators," in *Proc. 7th Int. Conf. Transducers*, Chicago, IL, 1997, pp. 45–48.
[8] H.-W. Kang, I. H. Lee, and D.-W. Cho, "Development of a micro-bellows actuator using micro-stereolithography technology," *Microelectron. Eng.*, vol. 83, no. 4–9, pp. 1201–1204, Apr.–Sep. 2006.
[9] K. H. Kim, H. J. Yoon, O. C. Jeong, and S. S. Yang, "Fabrication and test of a micro electromagnetic actuator," *Sens. Actuators A, Phys.*, vol. 117, no. 1, pp. 8–16, Jan. 2005.
[10] R. Luharuka, H. Noh, S. K. Kim, H. Mao, L. Wong, and P. J. Hesketh, "Improved manufacturability and characterization of a corrugated parylene diaphragm pressure transducer," *J. Micromech. Microeng.*, vol. 16, no. 8, pp. 1468–1474, Aug. 2006.
[11] Y.-K. Yoon, J.-H. Park, F. Cros, and M. G. Allen, "Integrated vertical screen microfilter system using inclined SU-8 structures," in *Proc. 16th Int. Conf. Micro Electro Mech. Syst.*, Kyoto, Japan, 2003, pp. 227–230.
[12] M. Han, W. Lee, S.-K. Lee, and S. S. Lee, "Fabrication of 3D microstructures with inclined/rotated UV lithography," in *Proc. 16th Int. Conf. Micro Electro Mech. Syst.*, Kyoto, Japan, 2003, pp. 554–557.
[13] K.-Y. Hung, H.-T. Hu, and F.-G. Tseng, "Application of 3D glycerol-compensated inclined-exposure technology to an integrated optical pick-up head," *J. Micromech. Microeng.*, vol. 14, no. 7, pp. 975–983, Jul. 2004.
[14] M. D. Giovanni, *Flat and Corrugated Diaphragm Design Handbook*. New York: Marcel Dekker, 1982, pp. 252–253.
[15] G. Yuan, X. Wu, Y.-K. Yoon, and M. G. Allen, "Kinematically-stabilized microbubble actuator arrays," in *Proc. 18th Int. Conf. Micro Electro Mech. Syst.*, Miami, FL, 2005, pp. 411–414.
[16] Y.-K. Yoon, J.-H. Park, and M. G. Allen, "Multidirectional UV lithography for complex 3-D MEMS structures," *J. Microelectromech. Syst.*, vol. 15, no. 5, pp. 1121–1130, Oct. 2006.
[17] D. Lapadatu, A. Pyka, J. Dziuban, and R. Puers, "Corrugated silicon nitride membranes as suspensions in micromachined silicon accelerometers," *J. Micromech. Microeng.*, vol. 6, no. 1, pp. 73–76, 1996.
[18] [Online]. Available: http://www.scscoatings.com/parylene_knowledge/specifications.cfm
[19] *ANSYS Documentation*.

**Xiaosong (Sharon) Wu** received the B.E. degree in polymer materials and engineering from the Beijing Institute of Petrochemical Technology, Beijing, China, in 1999 and the M.S. degree in polymer chemistry and physics from the University of Science and Technology of China (USTC), Hefei, China, in 2003. She is currently pursuing the Ph.D. degree in polymer engineering in the School of Polymer, Textile and Fiber Engineering, Georgia Institute of Technology, Atlanta.

She was a Research Engineer with the USTC High Tech Company. Her research interest is developing polymer microfabrication technology for MEMS devices. Currently, her research area focuses on micropneumatic actuators, piezoelectric multilayer actuator, solid-hydraulically amplified microvalve arrays, and advanced polymer micromolding processes.

**Guang Yuan** received the B.S. degrees in mechanical engineering and electrical engineering and the M.S. and Ph.D. degrees in mechanical engineering from Tsinghua University, Beijing, China, in 1995, 1997, and 2000, respectively.

From 1994 to 2000, she was with Tsinghua University, working on medium-resolution microaccelerometer and gyroscopes. From 2000 to 2004, she was with the Georgia Institute of Technology, Atlanta, as a Postdoctor on several MEMS projects. She is currently with the School of Electrical and Computer Engineering, Georgia Institute of Technology. Her research interests include microsensors, microfluidic actuators, and micromolding and various 3-D microstructure fabrication.

**Yong-Kyu Yoon** (S'03–M'03) received the B.S. and M.S. degrees in electrical engineering from the Seoul National University, Seoul, Korea, the MSEE degree from the New Jersey Institute of Technology, Newark, in 1999, and the Ph.D. degree in electrical and computer engineering from the Georgia Institute of Technology, Atlanta, in 2004.

He was a Postdoctoral Fellow with the Microelectronics Research Center, Georgia Institute of Technology. In 2006, he joined the State University of New York, Buffalo, as an Assistant Professor in the Electrical Engineering Department. His current research interests are 3-D MEMS fabrication; RF/Microwave components and devices such as inductors, capacitors, millimeter antennas, and waveguides; bio/microfluidic systems for the lab-on-a-chip; nanofabrication; microsensors and actuators; electronic and MEMS packaging; and ferroelectric material and its RF/optical applications.

**Mark G. Allen** (M'89–SM'04) received the B.A. degree in chemistry, the B.S.E. degree in chemical engineering, and the B.S.E. degree in electrical engineering from the University of Pennsylvania, Philadelphia, and the S.M. and Ph.D. degrees from the Massachusetts Institute of Technology, Cambridge.

Since 1989, he has been with the faculty of the Georgia Institute of Technology (Georgia Tech), Atlanta, where he holds the rank of Regents' Professor in the School of Electrical and Computer Engineering and the J. M. Pettit Professorship in Microelectronics, as well as a joint appointment in the School of Chemical and Biomolecular Engineering. He is also the Senior Vice Provost for Research and Innovation at Georgia Tech. His current research interests are in the field of microfabrication and nanofabrication technology, with emphasis on new approaches to fabricate devices with characteristic lengths in the micro- to nanoscale from both silicon and non-silicon materials. He is North American Editor of the *Journal of Micromechanics and Microengineering*.

Prof. Allen was the Cochair of the 1996 IEEE/ASME Microelectromechanical Systems Conference.